

1 Listening for the Mars 2020 Landing Sequence with InSight

2 **Listening for the Landing: Detecting Perseverance’s**
3 **landing with InSight**

4 **Benjamin Fernando¹, Natalia Wójcicka², Marouchka Froment^{3,4}, Ross**
5 **Maguire^{5,6}, Simon C. Stähler⁷, Lucie Rolland⁸, Gareth S. Collins², Ozgur**
6 **Karatekin⁹, Carene Larmat³, Eleanor K. Sansom¹⁰, Nicholas A. Teanby¹¹,**
7 **Aymeric Spiga^{12,13}, Foivos Karakostas⁵, Kuangdai Leng¹⁴, Tarje**
8 **Nissen-Meyer¹, Taichi Kawamura⁴, Dominico Giardini⁷, Philippe Lognonné⁴,**
9 **Bruce Banerdt¹⁵, Ingrid J. Daubar¹⁶**

10 ¹Department of Earth Sciences, University of Oxford, South Parks Road, Oxford, OX1 4AR, UK

11 ²Department of Earth Science and Engineering, Imperial College, London, SW7 2AZ, UK

12 ³Earth and Environmental Sciences Division, Los Alamos National Laboratory, Los Alamos, NM, USA

13 ⁴Université de Paris, Institut de Physique du Globe de Paris, CNRS, Paris, France

14 ⁵Department of Geology, University of Maryland, College Park, MD, USA

15 ⁶Department of Computational Mathematics, Science, and Engineering, Michigan State University, East
16 Lansing, MI, USA

17 ⁷Department of Earth Sciences, ETH Zurich, Sonneggstrasse 5, 8092 Zürich, Switzerland

18 ⁸Université Côte d’Azur, Observatoire de la Côte d’Azur, CNRS, IRD, Géoazur, France

19 ⁹Royal Observatory of Belgium, Belgium

20 ¹⁰Space Science and Technology Centre, Curtin University, Australia

21 ¹¹School of Earth Sciences, University of Bristol, Wills Memorial Building, Queens Road, Bristol BS8
22 1RJ, UK

23 ¹²Laboratoire de Météorologie Dynamique / Institut Pierre-Simon Laplace (LMD/IPSL), Sorbonne
24 Université, Centre National de la Recherche Scientifique (CNRS), École Polytechnique, École Normale

25 Supérieure (ENS), Campus Pierre et Marie Curie BC99, 4 place Jussieu 75005 Paris, France

26 ¹³Institut Universitaire de France (IUF), 1 rue Descartes, 75005 Paris, France

27 ¹⁴Scientific Computing Department, Rutherford Appleton Laboratory, Harwell, UK

28 ¹⁵Jet Propulsion Laboratory, California Institute of Technology, Pasadena, CA, USA

29 ¹⁶Earth, Environment and Planetary Sciences, Brown University, Providence, RI, USA

30 .

31 This manuscript is a pre-print. It has not been peer-reviewed and has been sub-
32 mitted to *JGR planets* for consideration.

Corresponding author: Benjamin Fernando, benjamin.fernando@seh.ox.ac.uk

33

Key Points:

34

- The entry, descent and landing of Mars 2020 (NASA's Perseverance Rover) will act as a seismic source on Mars which will have known temporal and spatial localization.

35

36

37

- We evaluate the detectability of the acoustic (atmospheric) and elastodynamic seismic (ground) signals, as well as the air-to-ground coupled signal, from this event at the location of NASA's InSight lander.

38

39

40

- We predict the atmospheric signal will not be detectable by InSight, but the seismic signal may be. A detection would be of enormous scientific value.

41

Abstract

The entry, descent, and landing (EDL) sequence of NASA’s Mars 2020 Perseverance rover will act as a seismic source of known temporal and spatial localization. We evaluate whether the signals produced by this event will be detectable at the InSight lander (3452 km away), comparing expected signal amplitudes to noise levels at the instrument. Modeling is undertaken to predict the propagation of the acoustic signal (purely in the atmosphere), the seismoacoustic signal (atmosphere-to-ground coupled), and the elastodynamic seismic signal (in the ground only). Our results suggest that the acoustic and seismoacoustic signals, produced by the atmospheric shockwave from the EDL, are unlikely to be detectable due to the pattern of winds in the martian atmosphere and the weak air-to-ground coupling, respectively. However, the elastodynamic seismic signal produced by the impact of the spacecraft’s cruise balance masses on the surface may be detected at InSight. The upper and lower bounds on predicted ground velocity at InSight are $1.0 \times 10^{-14} \text{ ms}^{-1}$ and $1.3 \times 10^{-10} \text{ ms}^{-1}$. The upper value is above the average noise floor at the time of landing 45% of the time. The uncertainties on this value reflect uncertainties in the current understanding of impact processes and translation of these into seismic signals. Uncertainty in the detectability also stems from the indeterminate instrument noise level at the time of this future event. A positive detection would be of great value in constraining the properties of the martian crust and mantle as well as in improving our understanding of impact-generated seismic waves.

Plain Language Summary

When it lands on Mars, NASA’s Perseverance Rover will have to slow down rapidly to achieve a safe landing. In doing this, it will produce a sonic boom, and eject two large balance masses which will hit the surface at very high speed. The sonic boom and balance mass impacts will produce seismic waves which will travel away from Perseverance’s landing site. Here we evaluate whether these seismic waves will be detectable at the location of InSight (3452 km away), and predict that the waves from the balance mass impacts may be detectable. If the waves are recorded by InSight, this would represent the first detection of ground motion generated by a seismic source on Mars at a known time and location. This would be of enormous value in advancing our understanding of the structure and properties of Mars’ atmosphere and interior.

1 Introduction**1.1 Motivation**

NASA’s InSight mission landed on Mars’ Elysium Planitia in November 2018, and since then has detected a number of ‘marsquake’ events which are thought to be geological in origin (Banerdt et al., 2020).

InSight faces a number of peculiar challenges associated with single-station seismology (Panning et al., 2015). Without independent constraints on source properties, robust seismic inversions are more challenging than they would be on Earth. Impact events (where meteoroids hit the planet’s surface) offer an opportunity to overcome some of these challenges as they can be photographically constrained in location, approximate timing, and size from orbital images. However, no impact events have yet been conclusively detected and identified using InSight’s seismometers, despite pre-landing expectations that impacts would make a significant contribution to martian seismicity (Daubar et al., 2018). A meteorite impact which formed a new 1.5 m impact crater only 37 km from InSight in 2019 was not detected (Daubar et al., 2020).

A number of possible reasons for the absence of impact detections thus far are apparent. These include uncertainties in the impactor flux entering Mars’ atmosphere (Daubar

et al., 2013) and in the seismic efficiency of ground impacts that form metre-scale craters (Wójcicka et al., 2020), as well as high ambient noise through much of the day, which makes detecting faint signals challenging. Should a seismic signal excited by an impact be detected, distinguishing it from tectonic events remains challenging due to intense scattering in the shallow crust of Mars (see van Driel et al. (2019) or Daubar et al. (2020) for further discussion).

If a seismic signal recorded by InSight could be identified as impact-generated, conclusive attribution to a particular spatial and temporal location would require identification of a new crater on the surface. Temporally sparse orbital imaging coverage of the martian surface, coupled with large error bounds on event distance and azimuth estimations (e.g. Giardini et al. (2020)) make this extremely challenging. This also excludes seismic signals induced by those impactors which either burn up or explode in the atmosphere as airburst events (Stevanović et al., 2017), and as such do not form new craters.

On Mars, a very limited number of events with known atmospheric entry ephemerides (meaning a priori known timings and locations) exist. The few that do occur are the entry, descent, and landing (EDL) sequences of human-made spacecraft. Whilst such detections have previously been achieved on Earth (de Groot-Hedlin et al., 2008), and spacecraft impact signals have been used as exemplar seismic sources on the Moon (Nunn et al., 2020), no seismic detection of an EDL on another planet has ever occurred. InSight’s potential to detect EDL sequences has, however, proved a source of inspiration in the popular media (*Away, Season 1, Episode 8*, 2020).

Such signals are of significant interest from a seismological point of view. If detected, they would enable us to both better constrain the seismic efficiency and impact processes for those bodies which strike the surface (as the incoming mass, velocity and angle are all known). They would also be of substantial benefit to planetary geophysics more generally, enabling us to calibrate the source and structural properties derived from other marsquake events which do not have a priori known source parameters. We also hope that the workflow developed here to evaluate the seismic detectability of EDL signals will be of use for future planetary seismology missions as well.

The next EDL sequence to occur on Mars will be that of NASA’s Mars 2020 (Perseverance) rover on February 18, 2021, which is the focus of this paper. We aim to estimate the amplitudes of the seismic signals this will produce at InSight’s location, and hence estimate their detectability.

1.2 The Mars 2020 EDL Sequence

Perseverance’s landing is targeted for approximately 15:00 Local True Solar Time (LTST) on February 18, 2021. This corresponds to 19:00 LTST at InSight ($4.50^\circ\text{N}/135.62^\circ\text{E}$, or roughly 20:00 UTC on Earth. The centre of the 10 km by 10 km landing ellipse is within Jezero Crater at $18.44^\circ\text{N}/77.50^\circ\text{E}$ (Grant et al., 2018). At atmospheric interface (125 km altitude), the spacecraft’s entry mass is 3350 kg.

This is a distance of 3452 km nearly due west from InSight. During descent the spacecraft trajectory is along an entry azimuth trajectory of approximately 100° (Figs. 1 and 2a), or pointing eastward and directed almost exactly towards InSight.

Two portions of the EDL sequence are likely to produce strong seismic signals. The first is the period during which the spacecraft is generating a substantial Mach shock as it decelerates in the atmosphere, and the second is the impact of the spacecraft’s two Cruise Mass Balance Devices (CMBDs) on the surface (note that six smaller balance masses which impact at much lower velocities are not appreciable seismic sources and are not considered in this paper).

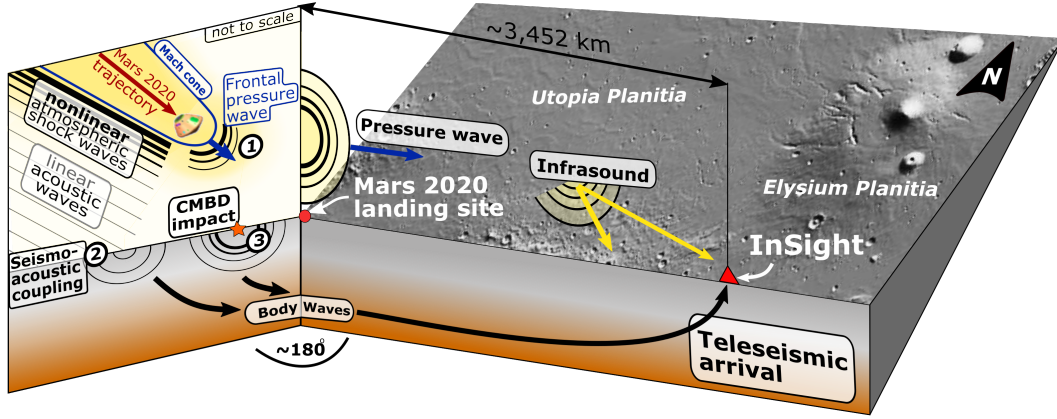


Figure 1. Schematic illustration of the seismic signals produced by the Mars 2020 EDL sequence (not to scale). Numbered features are: (1) the atmospheric acoustic signal, (2) the coupled seismoacoustic signal, and (3) the seismic signal propagating in the ground. The thickest airborne black lines represent non-linear shockwaves, decaying to weakly non-linear (thin black lines) and finally linear acoustic waves (thin gray lines). Surface waves, which on Mars do not appear to propagate at teleseismic distances, are not shown here. Black lines with single arrowheads represent body waves. The spacecraft’s trajectory at entry is eastward along an azimuth of 100° , almost exactly pointing toward InSight, i.e. the two panels are angled toward each other at nearly 180° , but are shown as they are here to acknowledge remaining uncertainties in the exact entry trajectory which exist at the time of writing. Note that this figure shows all three **potential** sources of seismic signal, and is not intended to suggest that these all reach InSight at detectable amplitudes.

138 The spacecraft will generate a sonic boom during descent, from the time at which
 139 the atmosphere is dense enough for substantial compression to occur (altitudes around
 140 100 km and below), until the spacecraft’s speed becomes sub-sonic, just under 3 min-
 141 utes prior to touchdown. This sonic boom will rapidly decay into a linear acoustic wave,
 142 with some of its energy striking the surface and undergoing seismoacoustic conversion
 143 into elastodynamic seismic waves, whilst some energy remains in the atmosphere and prop-
 144 agates as infrasonic pressure waves.

145 The CMBDs are dense, 77 kg unguided tungsten blocks which are jettisoned high
 146 in the EDL sequence (around 1,450 km above the surface). Due to their high ballistic
 147 coefficients, they are expected to undergo very limited deceleration before impact. Based
 148 on simulations and data from the Mars Science Laboratory Curiosity Rover’s EDL in
 149 2012, CMBD impact is expected to occur at about 4000 m/s, less than 100 km from the
 150 spacecraft landing site, and at about 10° elevation from the horizontal plane (Bierhaus
 151 et al., 2013). In the case of Curiosity, the CMBDs formed several craters between 4 and
 152 5 m in diameter, and the separation between CMBDs or their resulting fragments was
 153 no more than 1 km at impact (Bierhaus et al., 2013), implying a difference in impact time
 154 of less than 1 second.

155 **2 Methodology**

156 To assess their detectability at InSight, we consider three aspects of the signal gen-
 157 erated by Perseverance’s EDL. Corresponding to the labels in Fig. 1, these are:

- 158 1. Acoustic signal: A linear, acoustic wave propagating in the atmosphere as an in-
 159 frasonic (low frequency, <20 Hz) pressure wave, generated by the decay of the sonic
 160 boom produced during descent.
- 161 2. Coupled seismoacoustic signal: A coupled air-to-ground wave, produced by the
 162 sonic boom, or its linear decay product, impinging upon the surface and creating
 163 elastodynamic body waves. On Earth, this would usually produce detectable sur-
 164 face waves too - however on Mars these are rapidly scattered away to non-detectable
 165 levels and hence are not depicted here.
- 166 3. Elastodynamic signal: An elastodynamic wave ('conventional' seismic wave) trav-
 167 elling in the solid part of the planet, excited by the impact of the CMBDs.

168 In addition to the CMBDs, various other parts of the EDL hardware will impact
 169 the surface, including the heat shield, backshell and descent stage. However, in an op-
 170 timal landing scenario these are expected to be at sub-sonic speeds (less than 100 ms^{-1}
 171 for masses of 440, 600, and 700 kg respectively) and as such will not produce seismic sig-
 172 nals of comparable magnitude to the CMBD impact.

173 2.1 Acoustic signal

174 The shockwave produced by the hypersonic deceleration of the spacecraft will rapidly
 175 decay through viscous frictional processes into a linear acoustic wave. The resultant acous-
 176 tic (pressure) waves will propagate in the atmosphere following paths determined by the
 177 atmospheric structure. These acoustic wave trajectories are modelled using the WASP
 178 (Windy Atmospheric Sonic Propagation) software (Dessa et al., 2005). The propagation
 179 medium is a stratified atmosphere parameterised using a 1D effective sound speed. This
 180 effective sound speed accounts for the presence of directional waveguides in the atmo-
 181 sphere at certain times of day, caused by the vertical gradients of temperature and wind.
 182 Such waveguides can potentially enable long-distance propagation of an infrasonic sig-
 183 nal (Garcia et al. (2017), Martire et al. (2020)).

184 The adiabatic sound speed and horizontal wind speed along the great circle propa-
 185 gation path to InSight are computed from the Mars Climate Database (Millour et al.,
 186 2015), accounting for the variation in local time as the signal propagates (mid-afternoon
 187 at Mars 2020's landing site, early evening at InSight). Supplement Figs. S3 and S4 show
 188 the variation in effective sound speed with azimuth, highlighting that the effects of the
 189 wind are highly directional.

190 The atmospheric dust content, which significantly influences global wind and weather
 191 patterns through changes in opacity, is chosen as an average for the solar longitude L_s
 192 $=5^\circ$ (northern spring) season, in which dust storms are anyhow rare (Montabone et al.,
 193 2015).

194 Weather perturbations may cause second-order changes in the atmospheric con-
 195 ditions (Banfield et al., 2020), but would not change the overall dynamics of acoustic wave
 196 propagation considered here. Regardless, in general the martian atmosphere in the equa-
 197 torial regions in the northern spring is typically predictable in its meteorology (Spiga et
 198 al., 2018).

199 Infrasonic signals, if at detectable levels, would be recorded by InSight's APSS (Aux-
 200 iliary Payload Sensor Suite) instrument (Banfield et al., 2019).

201 2.2 Coupled seismoacoustic signal

202 The impact of the linear acoustic waves from the atmosphere (the products of the
 203 decaying shockwave) hitting the surface will excite elastodynamic (i.e. body and surface)
 204 waves in the solid ground. The crucial parameter which will determine the amplitude

of the elastodynamic waves in the solid ground is the air-to-ground coupling factor (which is a transmission coefficient).

Using the method of Sorrells et al. (1971), we estimate this factor by modelling the intersection of a planar acoustic wave with a regolith-like target material. Full details of the method are described in the Supplement (Text S1), however this value is found to be $4 \times 10^{-6} \text{ ms}^{-1} \text{ Pa}^{-1}$. It is thus possible to proceed to predicting amplitudes at InSight.

2.2.1 Surface waves

Modeling of the excitation of surface waves was discussed in detail by Lognonné et al. (2016) and Karakostas et al. (2018). However, the combination of a small transmission coefficient and strong seismic scattering in the portions of the crust where the surface waves propagate means that the surface wave signal is extremely unlikely to be detected at InSight and we do not consider it further in this paper.

2.2.2 Body Waves

We focus instead on the seismoacoustically coupled direct-arrival body waves (observed on Earth from EDL impacts by Edwards et al. (2007)), which travel through the deeper parts of the crust and mantle where reduced attenuation due to scattering is expected.

We use the methods of (ReVelle, 1976), adapted to martian conditions, to estimate the atmospheric overpressure (i.e. the strength of the infrasound pressure wave) which impacts upon the surface in the Perseverance landing region. Multiplying this value by the air-to-ground coupling factor gives an upper bound on the the velocity amplitude of the P-wave at the landing site.

The decay of this amplitude with distance to InSight’s position can then be calculated using either waveform modeling or scaling laws (these are discussed below). The S-wave amplitude from the coupled seismoacoustic signal is expected to be much smaller, as the vertical incidence of the atmospheric acoustic wave produces much stronger pressure perturbations than shear perturbations in the solid ground.

The resulting body waves propagating in the solid ground will, if large enough in amplitude, be detected by InSight’s SEIS (Seismic Experiment for Interior Structure) instrument (Lognonné et al., 2019).

2.3 Elastodynamic seismic signal

Two approaches are taken to estimate the amplitudes of the seismic waves produced by the CMBD impacts at InSight, and hence to evaluate their potential detectability by SEIS.

The dynamics calculations for the spacecraft’s re-entry prior to CMBD jettison, which confirm the CMBD impact parameters based on data from the Mars Science Laboratory in 2020, (Karlgaard et al., 2014) are also discussed in the Supplement.

2.3.1 Method 1: Empirical amplitude scaling relationships

The first approach uses the scaling relations of Teanby (2015) and Wójcicka et al. (2020) to estimate the peak P-wave amplitudes at InSight’s location. The amplitudes of the S-wave are significantly harder to estimate (and are not predictable from the published scaling relationships discussed below), but are likely to be of the same order of magnitude as the P-waves.

249 These relationships are both based on the measured P-wave amplitudes as a func-
 250 tion of distance from artificial lunar (Latham, Ewing, et al., 1970) and terrestrial mis-
 251 sile impact experiments (Latham, McDonald, & Moore, 1970), but apply different ap-
 252 proaches to the scalings themselves.

253 Full details of the differences between these approaches are included in the Sup-
 254 plementary Information. In summary, the Teanby (2015) approach scales an empirically
 255 derived P-wave amplitude with the square root of the impactor’s kinetic energy; whilst
 256 Wójcicka et al. (2020) uses a scaling based on impactor momentum. These both yield
 257 a predicted P-wave amplitude at InSight’s positions. In both cases, the scaling of peak
 258 P-wave amplitude with distance from the source r follows a $r^{-1.6}$ relationship empiri-
 259 cally which is derived from controlled source experiments.

260 The application of lunar and terrestrial-derived scaling relationships to Mars is well-
 261 established (e.g. Daubar et al. (2020)). However, it should be noted that both these ap-
 262 proaches involve extrapolation in distance to reach the 3452 km separation to InSight.
 263 Extrapolation is required because comparable (i.e., controlled-source, and with the same
 264 momentum and energy) impact events have not previously been recorded on the Moon
 265 or Earth at distances greater than 1200 km.

266 The estimated impact energy, total momentum, and vertical-component momen-
 267 tum of the CMBD impact are 6×10^8 J, 3×10^5 N s, and 5.2×10^4 N s respectively.

268 **2.3.2 Method 2: Wave propagation modeling using estimated moments**

269 The second approach predicts the amplitudes of the elastodynamic waves recorded
 270 at InSight using wave propagation modeling. Because elastodynamic wave propagation
 271 is linear, the amplitude at InSight is directly proportional to the magnitude of the source,
 272 and calculations can be easily re-scaled for different estimates of source magnitude (which
 273 in these cases is a seismic moment) to yield a range of predicted amplitudes.

274 The seismic moment is thus the primary determinant. Several approaches have been
 275 proposed to estimate the seismic moment of an impact, with an uncertainty that spans
 276 two orders of magnitude (Daubar et al., 2018). Here we derive two independent estimates
 277 of the seismic moment: (A) using the seismic moment scaling relation of Teanby and Wookey
 278 (2011), and (B) using impact physics modeling codes to simulate the non-linear plastic
 279 behaviour and relevant shock physics at the CMBD impact site.

280 **A) Scaling-based moment estimates** Rearranging equations (5) and (6) of
 281 Teanby and Wookey (2011) provide an empirically-derived relationship between seismic
 282 moment (M) and impact kinetic energy (E), via $M = (k_s E / 4.8 \times 10^{-9})^{0.81}$, where k_s
 283 is the seismic efficiency of the impact. While there remains considerable uncertainty in
 284 the most appropriate value for the seismic efficiency of small impacts on Mars (Teanby
 285 & Wookey, 2011; Daubar et al., 2018; Wójcicka et al., 2020), to derive a plausible up-
 286 per bound on the seismic moment of the CMBD impact we adopt a value of $k_s = 5 \times$
 287 10^{-4} (Teanby, 2015; Daubar et al., 2018), which yields a seismic moment $M = 1.3 \times$
 288 10^{11} Nm. This estimate has at least an order of magnitude uncertainty.

289 **B) Impact physics hydrocode simulations** To estimate the seismic moment
 290 of the CMBD impact in an independent way we use the iSALE2D (Amsden et al., 1980;
 291 Collins et al., 2004; Wünnemann et al., 2006) and HOSS (Munjiza, 2004; Lei et al., 2014;
 292 Knight et al., 2020) impact physics codes to simulate the impact and wave generation
 293 process on millisecond timescales. Realistic simulations of highly oblique impacts such
 294 as the M2020 CMBD impact are extremely challenging. Whilst HOSS is capable of such
 295 simulations (iSALE2D is not), these are executable only with lower spatial resolution and
 296 over a shorter duration than simulations with vertical impactors.

Therefore, to provide the most robust prediction possible, we both simulated the CMBD impact as a vertical impact of the same momentum magnitude (3×10^5 Ns) using both iSALE2D and HOSS, and also simulated its actual highly oblique geometry with HOSS at both a lower-resolution over a shorter duration.

This vertical impact simulation is expected to provide an upper bound on the seismic moment as it maximises the coupling of the impactor’s energy with the ground.

To estimate the seismic moment in the vertical impact case with iSALE we follow the approach described by Wójcicka et al. (2020). The shape of the CMBD in iSALE2D is approximated as a tungsten sphere of radius 9.6 cm and mass 75 kg. The mesh used in the simulations is cylindrically symmetric, approximately 30 m in radius. The impact-generated shockwave is tracked at high resolution until it decays to a purely linear elastodynamic wave. The target material is a porous basaltic regolith, approximating the local geological conditions at Jezero Crater. Its bulk density is $\rho = 1589$ kg/m⁻³ and sound speed is $c_B = 857$ m/s.

To replicate the iSALE simulation with HOSS and determine an independent estimate of the seismic moment, the HOSS model was configured with as close to the same initial conditions and material models as possible. The HOSS equation of state for this porous material takes the form of a user-defined curve relating pressure and volumetric strain and was validated for laboratory-scale impact experiments in a martian regolith simulant (Froment et al., 2020; Richardson & Kedar, 2013). Further details of the iSALE and HOSS modeling are provided in the supplementary information and a comparison between iSALE and HOSS respective parameters can be found in Supplement Table S1.

The scalar seismic moment of the impact was calculated in differently for the different simulation approaches. The scalar seismic moment calculated from the iSALE simulation results uses a combination of three methods (Wójcicka et al., 2020) that each provide a measure of either the scalar seismic moment or the diagonal components of the full seismic moment tensor. The method used to determine the seismic moment from the HOSS simulation provides information about the full seismic moment tensor, including off-diagonal terms. Further details are provided in the Supplement.

Wave propagation modeling Synthetic waveforms with an isotropic source are generated using Instaseis (van Driel et al., 2015) to retrieve pre-computed Green’s function databases prepared for the InSight mission (Ceylan et al., 2017). These are accurate up to a frequency of 1 Hz. These are then rescaled using the moments, derived as detailed above.

In this paper, we consider the structural model EH45TcoldCrust1 (Rivoldini et al., 2011), which has been used in previous benchmark modeling of impact signals on Mars (Daubar et al., 2018). While modelled waveform amplitudes vary slightly between different structural models, the variations associated with different models are far lower than the uncertainty of the estimated seismic moment of the impact. Given the uncertainties in modeling the focal mechanism for a hypersonic impact (see Daubar et al. (2018) for more details), the use of an isotropic (explosive) source is a standard and justifiable assumption.

3 Results

3.1 Acoustic signal

Fig. 2 presents ray-tracing simulations. The acoustic energy release at any point in time is dependent on both the velocity of the entry vehicle and the atmospheric density (and hence, the spacecraft altitude). The point of maximum energy release occurs

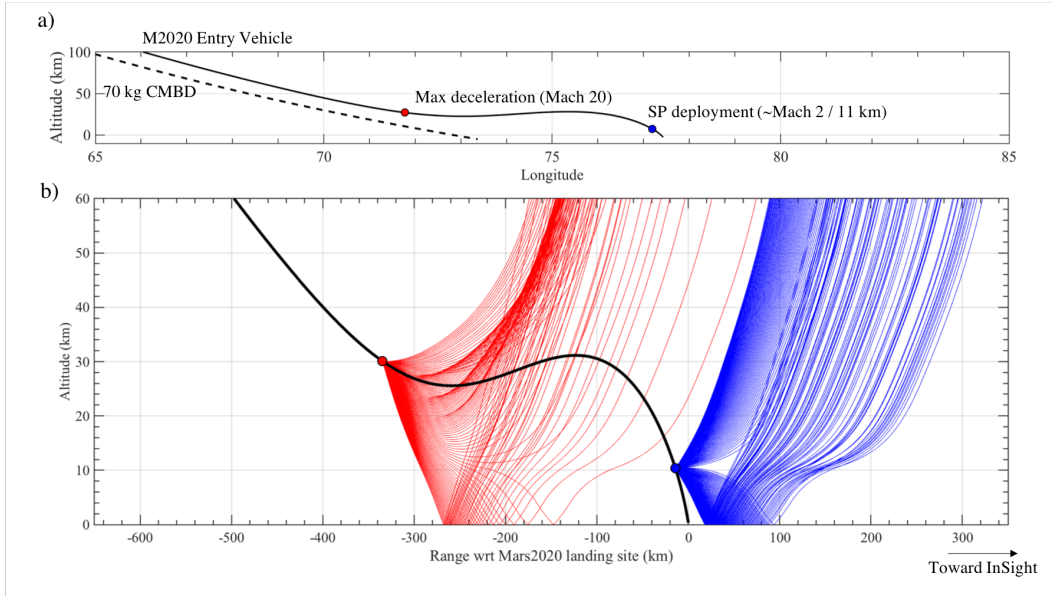


Figure 2. Panel a) shows the entry trajectories of the CMBDs and Mars 2020 entry vehicle (solid and dashed curves, respectively) CMBD separation occurs far off to the top left of the graphic (~ 1450 km altitude and ~ 3330 km downrange). The red disk marks the calculated point of maximum of deceleration (where the emission of acoustic energy into the atmosphere is highest) and the blue disk marks the estimated location of the Supersonic Parachute (SP) opening, after which the spacecraft rapidly becomes subsonic. Panel b) illustrates the infrasound propagation paths on Mars at the time of landing, in red for a source at 30 km height and in blue for an acoustic source at 11 km where the SP deployment occurs.

344 at the point of maximum aerodynamic deceleration, or approximately 30 km above the
 345 surface and 90 seconds after atmospheric entry interface.

346 Energy emitted at altitudes above 10 km, energy reflects off the surface back into
 347 the atmosphere at too steep an angle to propagate toward the lander. Therefore, the acous-
 348 tic signal produced around the time at which Mars 2020 is undergoing maximum decel-
 349 eration will not be detectable by InSight due to the geometry of the waveguide layer.

350 Below 10 km, acoustic energy from the decaying shock front may become trapped
 351 between the wind layers in the atmosphere and the surface, and hence propagate for long
 352 distances. However, the amount of acoustic energy emitted will decrease substantially
 353 as the entry vehicle’s parachute deploys and it passes into the subsonic regime, around
 354 140 s prior to landing and approximately 11 km above the surface.

355 As such, the acoustic signals emitted by the spacecraft decelerating within the wave-
 356 guide layer (between the surface and 10 km) will be extremely weak, and will not be de-
 357 tectable by InSight’s APSS instrument.

358 The impact of the CMBDs with the ground will generate a substantial acoustic sig-
 359 nal which will propagate up into the atmosphere. Due to the complexities of this signal’s
 360 generation and propagation, it is not currently possible to meaningfully estimate its am-
 361 plitude at InSight’s position. However, given that it will be much higher-frequency than
 362 the acoustic signal produced by the entry vehicle’s deceleration, the signal will be rapidly
 363 attenuated by the high CO₂ concentration in the martian atmosphere. As such, the this
 364 infrasound signal is not expected to be detectable at InSight’s position either.

365 **3.2 Seismoacoustic coupled signal**

366 We estimate a maximum overpressure at ground level of 0.9 Pa, which is attributable
 367 to the portion of the sonic boom generated at 25 km height. At this position, the space-
 368 craft is travelling fast enough to still generate a substantial shockwave (Mach 15).

369 Using our calculated air-to-ground coupling factor of $4 \times 10^{-6} \text{ ms}^{-1} \text{ Pa}^{-1}$ this trans-
 370 lates into a ground deformation velocity of $3.6 \times 10^{-6} \text{ ms}^{-1}$ at the landing site. Mod-
 371 elling a seismic source of this magnitude using Instaseis suggests a maximum P-wave am-
 372 plitude no larger than $2 \times 10^{-11} \text{ m/s}$. The average noise spectrum is discussed below
 373 in Sec. 4.2, but in short this is substantially below the noise floor and hence will not be
 374 detectable.

375 **3.3 Elastodynamic seismic signal**

376 **3.3.1 Method 1: Empirical scaling relationships**

377 Application of the empirical scaling relationships (Teanby, 2015; Wójcicka et al.,
 378 2020) described in section 2.3.1 to the CMBD impact results in a range of peak P-wave
 379 velocities at the distance of InSight of between 2.1×10^{-12} and $1.3 \times 10^{-10} \text{ ms}^{-1}$ (Fig. S1).
 380 An extrapolation of the Teanby (2015) scaling on its own gives a predicted ground ve-
 381 locity of $5_{-3.5}^{+10} \times 10^{-11} \text{ ms}^{-1}$. However the actual uncertainties on these values are likely
 382 to be somewhat larger as the CMBD impact range of 3452 km is well beyond the range
 383 of the data used to develop the scaling (<1200 km). These results are plotted and com-
 384 pared to other derived values in Fig. 3.

385 **3.3.2 Method 2: Wave propagation modeling with an estimated seismic 386 moment**

387 In the case where the impact of one CMBD is approximated as a vertical impact,
 388 iSALE2D predicts a scalar seismic moment of $5.85 \pm 1.5 \times 10^8 \text{ Nm}$ whilst HOSS pre-

389 predicts a moment of $1.79 \times 10^9 \text{ Nm}$. The factor-of-three discrepancy between these two val-
 390 ues is likely due to differences in the way that the ejecta from the CMBD crater is mod-
 391 elled and in how the surface material is parameterised. As described in the supplemen-
 392 tary material, each moment estimate was computed using a different mathematical ap-
 393 proach, which will also introduce discrepancy.

394 In the case of a highly oblique CMBD impact, the HOSS simulation results yield
 395 a scalar seismic moment of $0.76 \times 10^9 \text{ Nm}$, comparable to the scalar moment of the ver-
 396 tical impact approximation. We note, however, that in this case, the scalar seismic mo-
 397 ment is dominated by one off-diagonal component of the moment tensor (shear in the
 398 vertical and along-trajectory directions), whereas the diagonal terms of the moment ten-
 399 sor dominate in the vertical impact case (Table S2). This suggests that the use of an isotropic
 400 moment tensor source approximation in our wave propagation modeling to represent a
 401 highly oblique impact source may introduce an additional uncertainty in P-wave ampli-
 402 tude that should be explored in further work.

403 The combined estimates of scalar seismic moment suggest an approximate moment
 404 of $\sim 1 \times 10^9 \text{ Nm}$. While this estimate is more than two orders of magnitude less than
 405 the estimate of $1.3 \times 10^{11} \text{ Nm}$ based on the impact energy-moment scaling relationship
 406 of Teanby and Wookey (2011) (using an assumed k_s of 5×10^{-4}), it is consistent with other
 407 estimates of seismic moment (in both value and difference from other estimates) for im-
 408 pacts of similar momentum (Gudkova et al., 2015; Daubar et al., 2018; Wójcicka et al.,
 409 2020). We therefore consider a predicted range for the seismic moment of $1.0 \times 10^9 -$
 410 $1.3 \times 10^{11} \text{ Nm}$, which we are confident bounds the ‘true’ seismic moment, for scaling
 411 the results of our wave propagation modeling.

412 Using these limits on the source moment to linearly re-scale seismogram velocity
 413 amplitudes as discussed in Sec 2.3.2 yields amplitudes in the range $1.3 \times 10^{-12} \text{ ms}^{-1}$
 414 (corresponding to the upper bound predicted moment of $1.3 \times 10^{11} \text{ Nm}$) and $1.0 \times 10^{-14} \text{ ms}^{-1}$
 415 (corresponding to the lower bound of $1.0 \times 10^9 \text{ Nm}$). These upper and lower values (v_u
 416 and v_l) bound a predicted range of amplitudes. Seismograms, showing these amplitudes
 417 as well as approximate arrival times, are shown in the supplementary material, Fig. S2.

418 Possible reasons for the differences between the estimates produced by the direct
 419 scaling relationships and those produced using an intermediate wave propagation step
 420 are discussed below.

421 4 Discussion

422 4.1 Noise conditions

423 As discussed above, the acoustic and coupled air-to-ground seismoacoustic signals
 424 from Perseverance’s EDL will not be detectable at InSight’s location due to the geomet-
 425 rical constraints imposed by the atmospheric stratification.

426 However, in the case of the CMBD impact, the upper range of the amplitude pre-
 427 dictions from the scaling relationships and wave propagation/wave generation exceeds
 428 the noise floor for InSight’s SEIS instruments at certain times of day. We now consider
 429 how likely this signal is to exceed a signal-to-noise ratio of 1.5 (a reasonable threshold
 430 for detection, based on InSight detections of tectonic events) at the predicted time of Per-
 431 severance’s landing.

432 Given the highly repeatable meteorological patterns on Mars in the absence of a
 433 global dust storm, we estimate the likely noise levels at the time of Perseverance’s land-
 434 ing (the local evening of February 18, 2021) using data averaged across twenty evenings
 435 from the same period the previous martian year (687 ± 10 Earth days previously, UTC
 436 Earth dates 2019/04/01 to 2019/04/20).

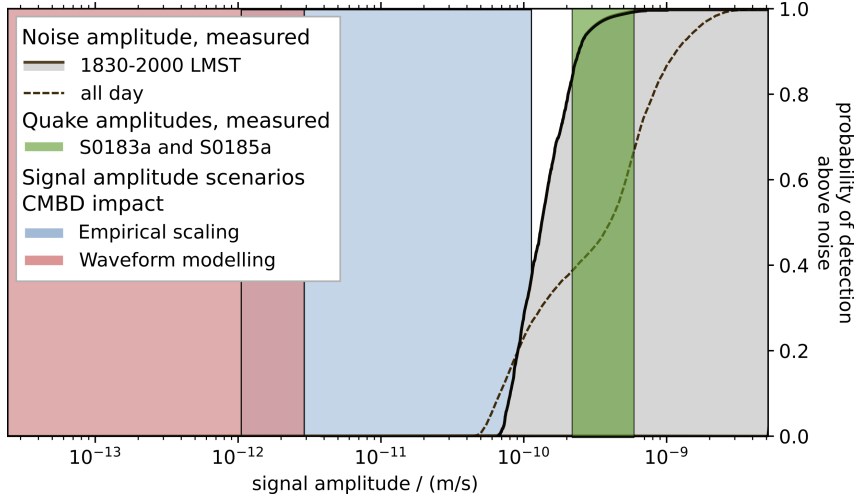


Figure 3. Detection probabilities for seismic signals of certain velocity amplitudes between 0.2 and 0.9 Hz. The solid black curve indicates the noise distribution considering the average signal amplitudes in only the early evening over 20 Sols during the same martian season in 2019, whilst the dashed black curve is for the whole period of 20 Sols. The shaded gray area indicates the regions in which signals are detectable. The blue and red bars mark the P-wave amplitude estimates of the 75-kg CMBD impact, using the empirical scaling and wave propagation modeling estimates, respectively, described earlier in this paper. Vertical lines bounding the different sectors correspond to the upper and lower bounds derived from these methods, for the blue and red sectors respectively (as an example, v_u and v_l are the vertical edges of the red sector). For comparison, the amplitudes of two tectonic marsquakes, S0183a and S0185a, located at comparable distance, are plotted in green.

437 In 2019, these spring evenings (18:30-20:00 LMST at InSight) on Mars were char-
 438 acterised by very low noise levels in the early evening post-sunset within the main seis-
 439 mic band used by the lander (0.2–0.9 Hz). To account for the temporal variability in the
 440 noise levels within this time, we consider the ‘probability’ of detection as being the frac-
 441 tion of time within the expected arrival window during which a signal of a given ampli-
 442 tude would be at least 1.5 times greater than the noise floor. For reference, we also plot
 443 the noise levels for the whole martian day (Sol) in Fig. 3; demonstrating that the noise
 444 is on average significantly lower during the evening.

445 4.2 Detection probabilities

446 The upper end of the peak amplitude estimates, derived from empirical impact scal-
 447 ing laws (Fig. S1), predicts an amplitude which exceeds the average early evening noise
 448 levels by a factor of 1.5 approximately 40% of the time. This implies that the elastody-
 449 namic signal propagating in the ground and induced by the CMBD impact may be de-
 450 tectable at InSight. However, the range of predicted peak ground velocities is substan-
 451 tial. This is not dissimilar to other amplitude predictions for martian impacts (Daubar
 452 et al., 2020). This is directly attributable to:

- 453 • Significant uncertainty in the efficiency of seismic wave generation of oblique im-
 454 pacts, especially in the relationship between impactor momentum and released seis-
 455 mic moment or between impact energy and seismic energy. This is partially a con-
 456 sequence of no impacts having been seismically detected on Mars to date.

- 457 • A lack of prior examples of hypersonic impacts detected at distances greater than
458 1200 km on any body, making calibrating scaling relationships challenging. Dif-
459 ferent approaches to extrapolating these, coupled with differences in material prop-
460 erties between terrestrial soils, lunar regolith and the martian surface, yield es-
461 timates that differ by two orders of magnitude depending on the choices made.
- 462 • The frequency bands used in estimating scaling relationships are not identical to
463 those used in waveform modeling and predicted noise levels. This is an unavoid-
464 able consequence of the frequency content of the available impact data, which are
465 observed at ranges less than 1200 km, so have a somewhat higher frequency con-
466 tent than we expect for the CMBD impacts. For example, the lunar impacts have
467 dominant frequencies of ~ 2 Hz, whereas we expect the optimal detection band with
468 the lowest noise is 0.2–0.9 Hz and waveform modeling is performed up to 1 Hz due
469 to computational limitations.

470 As the range in estimated peak amplitudes stems from a fundamental lack of ob-
471 served data in comparable contexts against which to check predictions and understand-
472 ing of the relevant processes, the range of estimates described here cannot be constrained
473 through further modeling. Rather, the uncertainties in our estimates reflect the general
474 lack of knowledge of the excitation and propagation over large distances of impact-generated
475 seismic waves.

476 Hence, even a single instance of impact detection from a source of known spatial
477 and temporal localisation would therefore be of enormous value. It would offer the po-
478 tential to better understand impact processes (especially seismic efficiency), enable us
479 to make headway in understanding the sub-surface geology at the landing site (through
480 placing constraints on its seismic properties), as well as offering constraints on the at-
481 tenuation and average propagation speed along the source-receiver path.

482 This strengthens the case for listening closely with InSight’s instruments for the
483 EDL sequence of Mars 2020. As the upper end of our certainly wide-ranging estimates
484 suggests a reasonable probability of a signal being detected, a positive detection would
485 go a long way to resolving the present uncertainty surrounding the propagation of the
486 elastodynamic waves generated by impacts. The enormous advantage that this event holds
487 in attempting to isolate its signal from the noise is that we know exactly the time and
488 location at which it will be produced, and can reasonably estimate when these signals
489 will reach InSight. A non-detection would similarly enable us to further constrain the
490 seismic detectability of impacts on Mars, though admittedly by a smaller margin than
491 a positive detection would.

492 5 Conclusions

493 We identified three possible sources of seismoacoustic signals generated by the EDL
494 sequence of the Perseverance lander: (1) the propagation of acoustic waves in the atmo-
495 sphere formed by the decay of the Mach shock, (2) the seismoacoustic air-to-ground cou-
496 pling of these waves inducing signals in the solid ground, and (3) the elastodynamic seis-
497 mic waves propagating in the ground from the hypersonic impact of the CMBDs.

498 In the first case (atmospheric propagation), the stratification and wind structure
499 in the atmosphere are such that the strongest signals produced will not be detectable
500 at InSight, as they are reflected off the ground back up into the atmosphere. Signals pro-
501 duced in the lower 10 km of the atmosphere may be trapped and propagate for long dis-
502 tances, however the spacecraft will be subsonic by this point and will not be emitting
503 substantial amounts of acoustic energy into the atmosphere. The Mach shock generated
504 higher in the atmosphere will also have largely dissipated by the time it propagates down
505 to this level. As such no detectable signal is expected.

506 In the second case (air-to-ground transmission), the coupling is expected to be very
 507 weak. Combined with the substantial distance to InSight, we predict a maximum ground
 508 velocity amplitude at SEIS’s position of $2 \times 10^{-11} \text{ ms}^{-1}$. This is well below the noise floor
 509 at all times of day and hence is not predicted to be detectable.

510 The impact processes in the third case (CMBD impact inducing seismic waves) are
 511 poorly constrained. Using a combination of scaling relationships and wave generation/wave
 512 propagation methods, we estimate that the direct body wave arrivals from the impact
 513 may be detectable at InSight. In the realistic best-case (and assuming identical weather
 514 and noise spectra to the same period one martian year earlier), the requisite signal-to-
 515 noise ratio would be sufficient for a positive detection 40% of the time. It should be noted
 516 that our modelling was for only one of the two CMBD impacts. Based on data from the
 517 Mars Science Laboratory (Curiosity) landing in 2012, the two CMBDs will impact around
 518 0.1 s and no more than 1 km apart. This separation is large enough that craters will not
 519 overlap and any interaction between the two signals will be in the linear propagation regime.
 520 As a result, the impact of two rather than one CMBD is unlikely to make a substantial
 521 difference to the observed signal, at best increasing the amplitude at InSight by a fac-
 522 tor of two.

523 Such a P-wave signal would present itself as a sharp peak in the ground velocity
 524 recorded by InSight’s SEIS instrument approximately 430 s after the impact of the CMBDs
 525 with the ground, just after 15:00 LMST (Perseverance time). If detectable, the S-wave
 526 signal would be expected some 300 s later; and the travel-time difference would be of use
 527 in identifying the signal.

528 This is likely to be the only impact event with known source parameters during the
 529 lifetime of the InSight mission. The Chinese Tianwen-1 is also expected to land on Mars
 530 in the spring of 2021 (Wan et al., 2020), but due to a lack of published information on
 531 the EDL sequence and hardware, and the time and precise location of its landing, mak-
 532 ing predictions about the detectability of this signal is not possible; though we eagerly
 533 seek clarifying information.

534 As such, the case for listening for the Mars 2020 signal with InSight’s instruments
 535 at the highest possible sampling rates is clear

536 **Acknowledgments**

537 The InSight Impacts team is grateful to Richard Otero, Erisa Stille, and Ian Clark of
 538 the Jet Propulsion Laboratory for their assistance in modeling and understanding the
 539 EDL process. BF and TNM are supported by the Natural Environment Research Coun-
 540 cil under the Oxford Environmental Research Doctoral Training Partnership, and the
 541 UK Space Agency Aurora grant ST/S001379/1. Computational resources were supplied
 542 in part by TNM’s NERC/EPSC UK National Supercomputer (ARCHER) grant. NW
 543 and GSC’s research is funded by the UK Space Agency (Grants ST/S001514/1 and ST/T002026/1).
 544 SCS acknowledges support from ETH Zürich through the ETH+ funding scheme (ETH+02
 545 19-1: “Planet Mars”). NAT is funded by UK Space Agency Grants ST/R002096/1 and
 546 ST/T002972/1. MF and CL’s research is funded by the Center of Space and Earth Sci-
 547 ence of Los Alamos National Laboratory. This research used resources provided by the
 548 Los Alamos National Laboratory Institutional Computing Program, which is supported
 549 by the U.S. Department of Energy National Nuclear Security Administration under Con-
 550 tract No. 89233218CNA000001. French co-authors acknowledge the support of CNES
 551 and of ANR (MAGIS, ANR-19-CE31-0008-08) for SEIS science support. I.J.D. is sup-
 552 ported by NASA InSight Participating Scientist grant 80NM0018F0612. OK acknowl-
 553 edges the support of the Belgian Science Policy Office (BELSPO) through the ESA/PRODEX
 554 Program.

555 This paper constitutes InSight Contribution Number 191 and LA-UR-20-29568.

556 Seismograms displayed in the supplementary material use wavefield database method
 557 Instaseis (van Driel et al., 2015), which is freely and openly available online: <https://instaseis.net>.
 558 Data for reproducing hydrocode simulations is available at Wójcicka and Froment (2020).
 559 We gratefully acknowledge the developers of iSALE shock physics code used in wave gen-
 560 eration modeling (www.isale-code.de). Details of the WASP code used in simulation of
 561 atmospheric acoustic propagation can be found in (Dessa et al., 2005).

562 References

- 563 Amsden, A., Ruppel, H., & Hirt, C. (1980). *SALE: a simplified ALE computer*
 564 *program for fluid flow at all speeds* (Tech. Rep.). Los Alamos, NM (United
 565 States): Los Alamos National Laboratory (LANL). doi: 10.2172/5176006
 566 *Away, Season 1, Episode 8* (Tech. Rep.). (2020). Netflix.
 567 Backus, G., & Mulcahy, M. (1976a). Moment tensors and other phenomenologi-
 568 cal descriptions of seismic sources – I. Continuous displacements. *Geophysical*
 569 *Journal International*, 46(2), 341–361.
 570 Backus, G., & Mulcahy, M. (1976b). Moment tensors and other phenomenological
 571 descriptions of seismic sources – II. Discontinuous displacements. *Geophysical*
 572 *Journal International*, 47(2), 301–329.
 573 Banerdt, W. B., Smrekar, S. E., Banfield, D., Giardini, D., Golombek, M., Johnson,
 574 C. L., ... Wieczorek, M. (2020). *Initial results from the InSight mission on*
 575 *Mars* (Vol. 13). doi: 10.1038/s41561-020-0544-y
 576 Banfield, D., Rodriguez-Manfredi, J. A., Russell, C. T., Rowe, K. M., Leneman, D.,
 577 Lai, H. R., ... Banerdt, W. B. (2019). *InSight Auxiliary Payload Sensor Suite*
 578 *(APSS)* (Vol. 215). doi: 10.1007/s11214-018-0570-x
 579 Banfield, D., Spiga, A., Newman, C., Forget, F., Lemmon, M., Lorenz, R., ...
 580 Banerdt, W. B. (2020). The atmosphere of Mars as observed by InSight.
 581 *Nature Geoscience*, 13(3), 190–198. doi: 10.1038/s41561-020-0534-0
 582 Bierhaus, E., McEwen, A., Wade, D., & Ivanov, A. (2013, Apr). Lunar and planetary
 583 science conference, 2013..
 584 Ceylan, S., van Driel, M., Euchner, F., Khan, A., Clinton, J., Krischer, L., ... Gi-
 585 arardini, D. (2017). From Initial Models of Seismicity, Structure and Noise
 586 to Synthetic Seismograms for Mars. *Space Science Reviews*, 1–16. doi:
 587 10.1007/s11214-017-0380-6
 588 Collins, G. S., Melosh, H., & Wünnemann, K. (2011). Improvements to the $\epsilon - \alpha$
 589 porous compaction model for simulating impacts into high-porosity solar sys-
 590 tem objects. *International Journal of Impact Engineering*, 38(6), 434–439. doi:
 591 10.1016/j.ijimpeng.2010.10.013
 592 Collins, G. S., Melosh, H. J., & Ivanov, B. A. (2004). Modeling damage and de-
 593 formation in impact simulations. *Meteoritics & Planetary Science*, 39(2), 217–
 594 231. doi: 10.1111/j.1945-5100.2004.tb00337.x
 595 Daubar, I., Lognonné, P., Teanby, N. A., Collins, G. S., Clinton, J., Stähler, S., ...
 596 Banerdt, B. (2020, jul). A New Crater Near InSight: Implications for Seis-
 597 mic Impact Detectability on Mars. *Journal of Geophysical Research: Planets*,
 598 125(8). doi: 10.1029/2020JE006382
 599 Daubar, I., Lognonné, P., Teanby, N. A., Miljkovic, K., Stevanović, J., Vaubailon,
 600 J., ... Banerdt, W. B. (2018). Impact-Seismic Investigations of the InSight
 601 Mission. *Space Science Reviews*, 214. doi: 10.1007/s11214-018-0562-x
 602 Daubar, I., McEwen, A., Byrne, S., Kennedy, M., & Ivanov, B. (2013). The current
 603 martian cratering rate. *Icarus*, 225(1), 506–516. doi: 10.1016/J.ICARUS.2013
 604 .04.009
 605 de Groot-Hedlin, C. D., Hedlin, M. A. H., Walker, K. T., Drob, D. P., & Zumberge,
 606 M. A. (2008). Evaluation of infrasound signals from the shuttle Atlantis using
 607 a large seismic network. *The Journal of the Acoustical Society of America*,
 608 124(3), 1442. doi: 10.1121/1.2956475

- 609 Dessa, J. X., Virieux, J., & Lambotte, S. (2005). Infrasound modeling in a spherical
610 heterogeneous atmosphere. *Geophysical Research Letters*, *32*(12), 1–5. doi: 10
611 .1029/2005GL022867
- 612 Edwards, W. N., Eaton, D. W., McCausland, P. J., ReVelle, D. O., & Brown, P. G.
613 (2007). Calibrating infrasonic to seismic coupling using the Stardust sam-
614 ple return capsule shockwave: Implications for seismic observations of me-
615 teors. *Journal of Geophysical Research: Solid Earth*, *112*(10), 1–13. doi:
616 10.1029/2006JB004621
- 617 Froment, M., Rougier, E., Larmat, C., Lei, Z., Euser, B., Kedar, S., . . . Lognonné,
618 P. (2020). Lagrangian-based simulations of hypervelocity impact exper-
619 iments on Mars regolith proxy. *Geophysical Research Letters*, *47*(13),
620 e2020GL087393.
- 621 Garcia, R. F., Brissaud, Q., Rolland, L., Martin, R., Komatitsch, D., Spiga, A., . . .
622 Banerdt, B. (2017). Finite-Difference Modeling of Acoustic and Gravity Wave
623 Propagation in Mars Atmosphere: Application to Infrasonds Emitted by
624 Meteor Impacts. *Space Science Reviews*. doi: 10.1007/s11214-016-0324-6
- 625 Giardini, D., Lognonné, P., Banerdt, W. B., Pike, W. T., Christensen, U., Ceylan,
626 S., . . . Yana, C. (2020). The seismicity of Mars. *Nature Geoscience*, *13*,
627 205–212. doi: 10.1038/s41561-020-0539-8
- 628 Grant, J. A., Golombek, M. P., Wilson, S. A., Farley, K. A., Williford, K. H., &
629 Chen, A. (2018). The science process for selecting the landing site for
630 the 2020 mars rover. *Planetary and Space Science*, *164*, 106 - 126. doi:
631 <https://doi.org/10.1016/j.pss.2018.07.001>
- 632 Gudkova, T., Lognonné, P., Miljković, K., & Gagnepain-Beyneix, J. (2015). Impact
633 cutoff frequency–momentum scaling law inverted from Apollo seismic data.
634 *Earth and Planetary Science Letters*, *427*, 57–65.
- 635 Johnson, G. R., & Cook, W. H. (1983). A constitutive model and data from metals
636 subjected to large strains, high strain rates and high temperatures. *Proc. 7th*
637 *Int. Symp. on Ballistics, The Hague, Netherlands*.
- 638 Karakostas, F., Rakoto, V., Lognonné, P., Larmat, C., Daubar, I., & Miljković, K.
639 (2018, Nov 27). Inversion of meteor rayleigh waves on earth and modeling of
640 air coupled rayleigh waves on mars. *Space Science Reviews*, *214*(8), 127. doi:
641 10.1007/s11214-018-0566-6
- 642 Karlgaard, C. D., Kutty, P., Schoenenberger, M., Munk, M. M., Little, A., Kuhl,
643 C. A., & Shidner, J. (2014). Mars science laboratory entry atmospheric data
644 system trajectory and atmosphere reconstruction. *Journal of Spacecraft and*
645 *Rockets*, *51*(4), 1029-1047. doi: 10.2514/1.A32770
- 646 Knight, E. E., Rougier, E., Lei, Z., Euser, B., Chau, V., Boyce, S. H., . . . Froment,
647 M. (2020). HOSS: an implementation of the combined finite-discrete element
648 method. *Computational Particle Mechanics*, 1–23.
- 649 Latham, G., Ewing, M., Dorman, J., Press, F., Toksoz, N., Sutton, G., . . . Yates,
650 M. (1970). Seismic data from man-made impacts on the moon. *Science*,
651 *170*(3958), 620–626. doi: 10.1126/science.170.3958.620
- 652 Latham, G., McDonald, W. G., & Moore, H. J. (1970). Missile impacts as sources of
653 seismic energy on the moon. *Science*, *168*(3928), 242–245.
- 654 Lei, Z., Rougier, E., Knight, E., & Munjiza, A. (2014). A framework for grand scale
655 parallelization of the combined finite discrete element method in 2d. *Computa-*
656 *tional Particle Mechanics*, *1*(3), 307–319.
- 657 Lognonné, P., Banerdt, W. B., Giardini, D., Pike, W. T., Christensen, U., Laudet,
658 P., . . . Wookey, J. (2019). *SEIS: Insight’s Seismic Experiment for Internal*
659 *Structure of Mars* (Vol. 215). doi: 10.1007/s11214-018-0574-6
- 660 Lognonné, P., Karakostas, F., Rolland, L., & Nishikawa, Y. (2016). Modeling of
661 atmospheric-coupled rayleigh waves on planets with atmosphere: From earth
662 observation to mars and venus perspectives. *The Journal of the Acoustical*
663 *Society of America*, *140*(2), 1447-1468. doi: 10.1121/1.4960788

- 664 Lognonné, P., Le Feuvre, M., Johnson, C. L., & Weber, R. C. (2009). Moon mete-
665 oritic seismic hum: Steady state prediction. *Journal of Geophysical Research*,
666 *114*(E12), E12003. doi: 10.1029/2008JE003294
- 667 Lognonné, P., Mosser, B., & Dahlen, F. (1994). Excitation of jovian seismic waves
668 by the Shoemaker-Levy 9 cometary impact. *Icarus*, *110*(2), 180–195.
- 669 Lundborg, N. (1968). Strength of rock-like materials. *International Journal of*
670 *Rock Mechanics and Mining Sciences and*, *5*(5), 427–454. doi: 10.1016/0148
671 -9062(68)90046-6
- 672 Martire, L., Garcia, R. F., Rolland, L., Spiga, A., Lognonné, P. H., Banfield, D., ...
673 Martin, R. (2020, jun). Martian Infrasond: Numerical Modeling and Analysis
674 of InSight’s Data. *Journal of Geophysical Research: Planets*, *125*(6), 1–34. doi:
675 10.1029/2020JE006376
- 676 Millour, E., Forget, F., Spiga, A., Navarro, T., Madeleine, J.-B., Montabone, L., ...
677 MCD/GCM development Team (2015). The Mars Climate Database (MCD
678 version 5.2). *European Planetary Science Congress 2015*, *10*, EPSC2015-438.
- 679 Montabone, L., Forget, F., Millour, E., Wilson, R. J., Lewis, S. R., Cantor, B., ...
680 Wolff, M. J. (2015). Eight-year climatology of dust optical depth on Mars.
681 *Icarus*, *251*, 65–95. doi: 10.1016/j.icarus.2014.12.034
- 682 Müller, G. (1973). Seismic moment and long-period radiation of underground nu-
683 clear explosions. *Bulletin of the Seismological Society of America*, *63*(3), 847–
684 857.
- 685 Munjiza, A. (2004). *The combined finite-discrete element method*. Wiley.
- 686 Nunn, C., Garcia, R. F., Nakamura, Y., Marusiak, A. G., Kawamura, T., Sun, D.,
687 ... Zhu, P. (2020). Lunar Seismology: A Data and Instrumentation Review.
688 *Space Science Reviews*, *216*. doi: 10.1007/s11214-020-00709-3
- 689 Panning, M. P., Beucler, É., Drilleau, M., Mocquet, A., Lognonné, P., & Banerdt,
690 W. B. (2015). Verifying single-station seismic approaches using Earth-based
691 data: Preparation for data return from the InSight mission to Mars. *Icarus*,
692 *248*(242), 230–242. doi: 10.1016/j.icarus.2014.10.035
- 693 ReVelle, D. O. (1976, mar). On Meteor-Generated Infrasond. *Journal of Geophysi-
694 cal Research*, *81*(7), 1217–1230. doi: 10.1029/ja081i007p01217
- 695 Richardson, J., & Kedar, S. (2013). An experimental investigation of the seismic sig-
696 nal produced by hypervelocity impacts. In *Lunar and planetary science confer-
697 ence* (Vol. 44, p. 2863).
- 698 Rivoldini, A., Van Hoolst, T., Verhoeven, O., Mocquet, A., & Dehant, V. (2011).
699 Geodesy constraints on the interior structure and composition of Mars. *Icarus*,
700 *213*(2), 451–472. doi: 10.1016/j.icarus.2011.03.024
- 701 Sorrells, G. G., McDonald, J. A., Herrin, E., & Der, Z. A. (1971). Earth Motion
702 Caused by Local Atmospheric-Pressure Changes. *Geophysical Journal of the
703 Royal Astronomical Society*, *26*(1-4), 83–&.
- 704 Spiga, A., Banfield, D., Teanby, N. A., Forget, F., Lucas, A., Kenda, B., ...
705 Banerdt, W. B. (2018). Atmospheric Science with InSight. *Space Science
706 Reviews*, *214*(7). doi: 10.1007/s11214-018-0543-0
- 707 Stevanović, J., Teanby, N. A., Wookey, J., Selby, N., Daubar, I. J., Vaubaillon,
708 J., & Garcia, R. (2017). Bolide Airbursts as a Seismic Source for the 2018
709 Mars InSight Mission. *Space Science Reviews*, *211*(1-4), 525–545. doi:
710 10.1007/s11214-016-0327-3
- 711 Teanby, N. A. (2015). Predicted detection rates of regional-scale meteorite impacts
712 on Mars with the InSight short-period seismometer. *Icarus*, *256*, 49–62.
- 713 Teanby, N. A., & Wookey, J. (2011). Seismic detection of meteorite impacts on
714 Mars. *Physics of the Earth and Planetary Interiors*, *186*, 70–80. doi: 10.1016/
715 j.pepi.2011.03.004
- 716 Tillotson, J. H. (1962). *Metallic Equations of State for Hypervelocity Impact*. Gen-
717 eral Atomic.

- 718 van Driel, M., Ceylan, S., Clinton, J. F., Giardini, D., Alemany, H., Allam, A., ...
719 Zheng, Y. (2019). *Preparing for InSight: Evaluation of the blind test for*
720 *martian seismicity* (Vol. 90) (No. 4). doi: 10.1785/0220180379
- 721 van Driel, M., Krischer, L., Stähler, S. C., Hosseini, K., & Nissen-Meyer, T. (2015).
722 Instaseis: Instant global seismograms based on a broadband waveform
723 database. *Solid Earth*, 6, 701–717. doi: 10.5194/se-6-701-2015
- 724 Walker, J. D. (2003). Loading sources for seismological investigation of asteroids and
725 comets. *International Journal of Impact Engineering*, 29(1-10), 757–769. doi:
726 10.1016/J.IJIMPENG.2003.10.022
- 727 Wan, W. X., Wang, C., Li, C. L., & Wei, Y. (2020). *China's first mission to Mars*
728 (Vol. 4) (No. 721). doi: 10.1038/s41550-020-1148-6
- 729 Wójcicka, N., Collins, G. S., Bastow, I. D., Teanby, N. A., Miljković, K., Rajšić,
730 A., ... Lognonné, P. (2020). The seismic moment and seismic efficiency
731 of small impacts on Mars. *Journal of Geophysical Research: Planets*. doi:
732 10.1029/2020JE006540
- 733 Wójcicka, N., & Froment, M. (2020). *nwojcicka/listening-for-landing-SI: listening-*
734 *for- landing-SI*. Zenodo. Retrieved from [https://doi.org/10.5281/zenodo](https://doi.org/10.5281/zenodo.4291898)
735 [.4291898](https://doi.org/10.5281/zenodo.4291898) doi: 10.5281/zenodo.4291898
- 736 Wünnemann, K., Collins, G. S., & Melosh, H. (2006). A strain-based poros-
737 ity model for use in hydrocode simulations of impacts and implications for
738 transient crater growth in porous targets. *Icarus*, 180(2), 514–527. doi:
739 10.1016/J.ICARUS.2005.10.013